

THE PREFLIGHT PHOTOMETRIC CALIBRATION OF THE EXTREME-ULTRAVIOLET IMAGING TELESCOPE EIT

K. P. DERE¹, J. D. MOSES¹, J.-P. DELABOUDINIÈRE², J. BRUNAUD²,
C. CARABETIAN², J.-F. HOCHEDÉZ², X. Y. SONG², R. C. CATURA³, F. CLETTE⁴
and J.-M. DEFISE⁵

¹*E.O. Hulburt Center for Space Research, Naval Research Laboratory,
Washington DC, 20375-5320 U.S.A.*

²*Institut d'Astrophysique Spatiale, Université Paris XI, 91405 Orsay Cedex, France*

³*Lockheed Martin Palo Alto Research Laboratory, Palo Alto, CA 94304, U.S.A.*

⁴*Observatoire Royal de Belgique, Brussels, Belgium*

⁵*Centre Spatial de Liège, Angleur, Belgium*

(Received 29 September 1999; accepted 6 March 2000)

Abstract. This paper presents the preflight photometric calibration of the Extreme-ultraviolet Imaging Telescope (EIT) aboard the Solar and Heliospheric Observatory (SOHO). The EIT consists of a Ritchey–Chrétien telescope with multilayer coatings applied to four quadrants of the primary and secondary mirrors, several filters and a backside-thinned CCD detector. The quadrants of the EIT optics were used to observe the Sun in 4 wavelength bands that peak near 171, 195, 284, and 304 Å. Before the launch of SOHO, the EIT mirror reflectivities, the filter transmissivities and the CCD quantum efficiency were measured and these values are described here. The instrumental throughput in terms of an effective area is presented for each of the various mirror quadrant and filter wheel combinations. The response to a coronal plasma as a function of temperature is also determined and the expected count rates are compared to the count rates observed in a coronal hole, the quiet Sun and an active region.

1. Introduction

The Extreme-ultraviolet Imaging Telescope (EIT) on the Solar and Heliospheric Observatory (SOHO) spacecraft records images of the solar transition region and corona. SOHO was launched in December 1995 near solar minimum. The EIT obtained its first images of the Sun on 2 January 1996 and has operated nearly continuously since that time. The intent of this paper is to present the results of the preflight photometric calibration so that EIT observations can be used as a reliable diagnostic of the temperature and density structure of the solar atmosphere.

The EIT has been described in detail by Delaboudinière *et al.* (1995). Briefly, the EIT consists of a Ritchey–Chrétien telescope with a CCD detector and several filters. An image of the complete Sun out to $1.4 R_{\odot}$ is recorded on a 1024^2 CCD detector with a resolution of 2.6 arc sec. per pixel. The multilayer coatings on the primary and secondary mirrors provide high reflectivity in narrow bands at EUV wavelengths. The mirror coatings have been applied in quadrants and different



Report Documentation Page				Form Approved OMB No. 0704-0188	
Public reporting burden for the collection of information is estimated to average 1 hour per response, including the time for reviewing instructions, searching existing data sources, gathering and maintaining the data needed, and completing and reviewing the collection of information. Send comments regarding this burden estimate or any other aspect of this collection of information, including suggestions for reducing this burden, to Washington Headquarters Services, Directorate for Information Operations and Reports, 1215 Jefferson Davis Highway, Suite 1204, Arlington VA 22202-4302. Respondents should be aware that notwithstanding any other provision of law, no person shall be subject to a penalty for failing to comply with a collection of information if it does not display a currently valid OMB control number.					
1. REPORT DATE 2000		2. REPORT TYPE		3. DATES COVERED 00-00-2000 to 00-00-2000	
4. TITLE AND SUBTITLE The Preflight Photometric Calibration of the Extreme-Ultraviolet Imaging Telescope EIT				5a. CONTRACT NUMBER	
				5b. GRANT NUMBER	
				5c. PROGRAM ELEMENT NUMBER	
6. AUTHOR(S)				5d. PROJECT NUMBER	
				5e. TASK NUMBER	
				5f. WORK UNIT NUMBER	
7. PERFORMING ORGANIZATION NAME(S) AND ADDRESS(ES) Naval Research Laboratory, 4555 Overlook Avenue SW, Washington, DC, 20375				8. PERFORMING ORGANIZATION REPORT NUMBER	
9. SPONSORING/MONITORING AGENCY NAME(S) AND ADDRESS(ES)				10. SPONSOR/MONITOR'S ACRONYM(S)	
				11. SPONSOR/MONITOR'S REPORT NUMBER(S)	
12. DISTRIBUTION/AVAILABILITY STATEMENT Approved for public release; distribution unlimited					
13. SUPPLEMENTARY NOTES					
14. ABSTRACT see report					
15. SUBJECT TERMS					
16. SECURITY CLASSIFICATION OF:			17. LIMITATION OF ABSTRACT Same as Report (SAR)	18. NUMBER OF PAGES 32	19a. NAME OF RESPONSIBLE PERSON
a. REPORT unclassified	b. ABSTRACT unclassified	c. THIS PAGE unclassified			

coatings applied in each quadrant to select four wavelength bands near 171, 195, 284, and 304 Å. A selector wheel at the front of the telescope selects one of four quadrants at a time. Several filters are included in the instrument design: entrance filters, filters on a filter wheel, and a final stray light filter immediately in front of the CCD detector. The elements considered in the calibration presented here include primarily the filter transmissions and the mirror reflectivities as a function of wavelength.

The calibration data were obtained during a series of measurements at the Orsay synchrotron. Many of these measurements have already been presented in the PhD. thesis of Song (1995). Defise *et al.* (1995) have also presented EIT calibration information. In the present analysis, models of the filters and mirrors are constructed to help understand their response over a wide range of wavelengths. Because of the effect of the Sun's radiation on the instrument itself, the throughput of the EIT is known to degrade (Defise *et al.*, 1995). However, this topic will not be addressed here.

2. The EIT Optics

A schematic of the EIT optical layout is shown in Figure 1. The sector wheel selects a single wavelength sector. The area of the entrance aperture is determined by two filter support grid structures for each sector and the coated area of the primary mirror. The entrance filters consist of thin aluminum coatings on both sides of a celluloid film supported on a metal grid. Of the five filters on the filter wheel, two are thin aluminum filters which block roughly half of the filter aperture. These are rarely used and are not considered here. The remaining three filters on the filter wheel include a clear aperture, an aluminum/celluloid filter as on the entrance aperture, and a pure aluminum filter. The stray-light (CCD) filter is also constructed of pure aluminum. The aluminum/celluloid filters nominally consist of a film of celluloid 500 to 700 Å thick with a 1000 to 1500 Å layer of aluminum deposited on both sides. The exposed aluminum is expected to develop an Al₂O₃ layer 20 to 50 Å deep. The pure aluminum filters nominally consist of 1500 Å foils, also with oxide layers on both sides.

The mirrors use Mo/Si multilayer coatings on their surfaces to attain high reflectivities in relatively narrow wavelength bands. These wavelength bands and other pertinent information are listed in Table I. Again, the primary and secondary mirrors are divided into quadrants, each with different coating specifications.

The detector is a 1024² back-illuminated SITe CCD that has been treated for improved quantum efficiency at EUV wavelengths.

TABLE I
EIT wavelength bands

Wavelength (Å)	Dominant ion	Characteristic temperature
171 Å	Fe IX, X	9×10^5 K
195 Å	Fe XII	1.3×10^6 K
284 Å	Fe XV	2×10^6 K
304 Å	He II	8×10^4 K

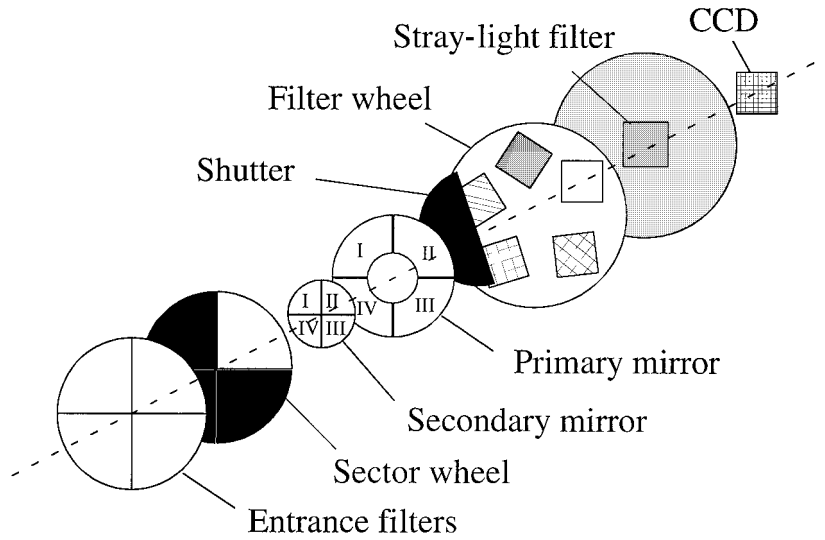


Figure 1. Optical elements of the EIT.

3. Calibration Setup

The SUPER-ACO synchrotron at Orsay provided a flux of EUV photons for the EIT calibration presented here. A monochromator was connected to the synchrotron by an evacuated line. The monochromator consisted of an entrance and exit mirror and a grating. One of two gratings could be selected for use in the monochromator. In addition, an aluminum or tin filter could be placed in the beam. The flux of photons incident at the EIT optics was determined by means of a silicon photodiode calibrated by NIST (Canfield, Kerner, and Korde, 1989).

TABLE II
EIT entrance filter models

Sector	Filter	Al ₂ O ₃	Al	Celluloid
171 Å	I1	30 Å	1500 Å	500 Å
171 Å	I2	30 Å	1500 Å	500 Å
195 Å	L1	30 Å	1900 Å	500 Å
195 Å	L2	30 Å	1900 Å	800 Å
284 Å	A1	30 Å	1500 Å	700 Å
284 Å	A2	30 Å	1500 Å	600 Å
304 Å	O1	30 Å	1500 Å	400 Å
304 Å	O2	30 Å	1500 Å	400 Å

4. Measurements of the Filter Transmissions

4.1. ENTRANCE FILTERS

Each mirror quadrant uses two entrance filters supported by two grids that also delineate the entrance aperture. The open area of each of these grids is 12 cm². However, since only a portion of the entrance aperture is seen by the multilayer coated portion of the primary mirror, the effective open aperture is 11.97 cm² for each quadrant. The transmission of the grid mesh supporting the filters is 94%.

The transmission of the filters was measured by placing each filter in the beam of EUV photons from the monochromator, scanning the monochromator in wavelength, and measuring the current in a photodiode which detected the number of photons that pass through the filter. This procedure was repeated with the filter removed from the beam so that the ratio of the currents in the photodiode would yield the transmission of each filter. One source of error in these measurements is associated with the amplifier measuring the photodiode currents. Immediately after an amplifier range change, the reported currents were often in error. In general, a series of measurements was performed with both gratings (R1 and R2) in the monochromator. A list of the filters is presented in Table II.

Figure 2 shows the calibration data for the 171 Å I1 filter. In the top left, a graph displays the photodiode currents measured with the filter in and out of the beam with grating No. 1 in the monochromator. The ratio of these two currents is the transmission which is plotted as a solid line in the bottom panel. A similar treatment is applied to data for monochromator grating No. 2 in the top right and bottom panels. The diamonds in the bottom panel refer to data obtained during observations of the Sun on SOHO with the aluminum/celluloid filter ‘Al+2’ on the filter wheel. This data was obtained by taking the ratio of the solar intensity with the filter in the clear and in the ‘Al+2’ position. The ‘Al+2’ filter is not the same

TABLE III
EIT filter-wheel and stray-light filters

Filter wheel filters						
Filter	Label	Name	Al ₂ O ₃	Al	Celluloid	Measurements
Open	Clear
Aluminum	Al+1	SQ35	50 Å	1500 Å	...	304, 584 Å
Aluminum	Al+2	SQC8	50 Å	1900 Å	400 Å	1 Wavelength scan + celluloid
Stray-light (CCD) filter						
Aluminum		SQ37	50 Å	1500 Å	...	171, 304, 584 Å

as the I1 filter but should be similar so that these observations provide a check on the synchrotron measurements. The squares are measurements performed by Physikalisch-Technische Studien (PTS). Similar measurements have been analyzed for all of the entrance filters.

The dashed line is a model calculation for a filter that consists of 500 Å of celluloid between two 1500 Å layers of aluminum with oxide layers of 30 Å. The filters have been modeled with the IMD database of Windt (1998), available at <http://www.bell-labs.com/user/windt/idl>. Celluloid consists of roughly 75% cellulose dinitrate (C₁₂H₁₈N₂O₁₄) and 25% camphor (C₁₀H₁₆O) which we have modeled as (C₁₂H₁₈N₂O₁₁) at a density of 1.2 g cm⁻³. This model filter approximates the measured transmission of the I1 filter and will be used in calculations of the combined instrument response. It has not been derived through a fitting process but has been selected as a combination that reasonable approximates the measurements. A list of the model parameters derived from measurements of each filter is given in Table II. The models suggest that there is significant variation of the thicknesses of the various layers from filter to filter.

4.2. FILTER-WHEEL FILTERS

The filter wheel has 5 filter positions. Two of these positions contain aluminum filters which cover only two-thirds of the filter opening, the remaining third being masked. These are only rarely used and will not be included here. The other filter-wheel apertures contain a clear aperture, an aluminum/celluloid filter, and a pure aluminum filter.

The synchrotron measurements of the transmission of the pure aluminum filter 'Al+1' in filter wheel do not currently exist. However, the transmission was measured at 304 and 584 Å by PTS. These measurements are shown in Figure 3. In addition, the transmission can be determined by comparing solar intensities ob-

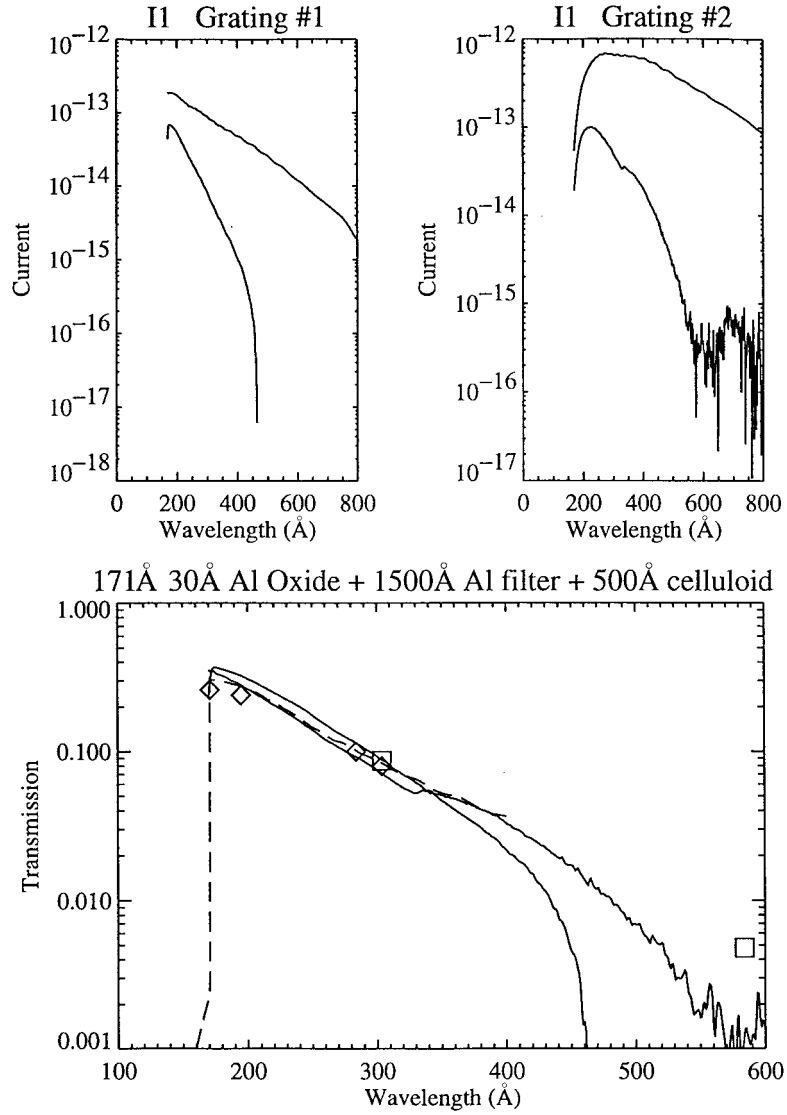


Figure 2. Calibration data for the 171 Å I1 filter transmission. *Top left*: photodiode currents with grating 1 in the monochromator; *top right*: photodiode currents with grating 2 in the monochromator. *Bottom*: the transmissions derived from the photodiode currents (*solid lines*), a model of the filter (*dashed line*), in-flight measurements with the 'Al+2' filter on the filter wheel (*diamonds*) and measurements performed by PTS (*squares*).

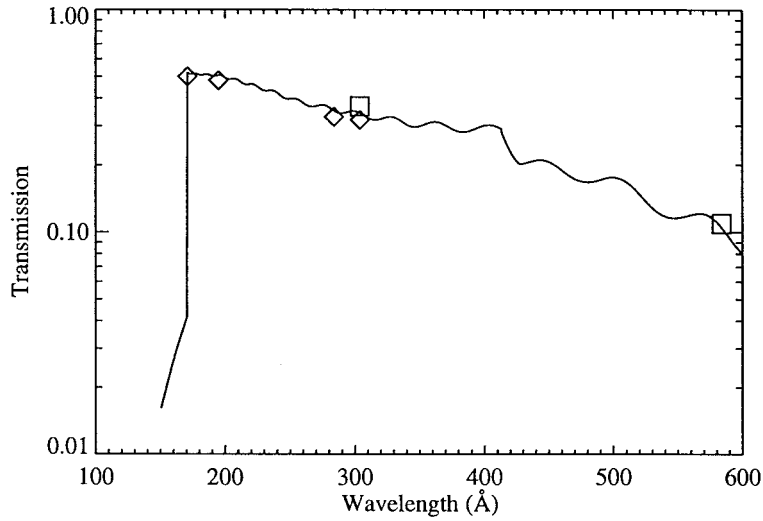


Figure 3. Calibration data for the 'Al+1' filter-wheel filter. In-flight measurements with the 'Al+1' filter on the filter wheel (diamonds), measurements performed by PTS (squares), and a model of the filter (dashed line).

served through the clear and 'Al+1' filter-wheel position for exposures separated by a small time interval. These measurements were made for all 4 EIT sectors. A model of the filter, as specified in Table III, is also plotted in Figure 3. The model calculations include the 83% transmission of the grid that they are mounted on.

For the 'Al+2' aluminum/celluloid filter mounted on the filter wheel, a single wavelength scan of calibration data is available. This data is plotted in the top right portion of Figure 4 together with the transmission derived from the ratio of the photodiode currents in the bottom of Figure 4. Also shown are PTS measurements reported by Song (1995), the transmission values derived from observations of the Sun with the 'Al+2' filter in and out of the beam, and the modeled transmission corresponding to the model values listed in Table III.

4.3. THE CCD STRAY-LIGHT FILTER

The stray-light filter SQ37 in front of the EIT CCD was measured only at 171, 304, and 584 Å. These measurements place the transmission of the stray-light filter between similar measurements of the SQ30 and SQ34 aluminum filters which were measured with complete wavelength scans. The measurements of these 2 filters, which can be modeled as 1300 Å and 1500 Å thick aluminum filters, respectively, are shown in the top of Figure 5. The model calculations include the 83% transmission of the grid that they are mounted on. The best model for the SQ37 CCD stray light filter is a 1500 Å aluminum foil with a 50 Å oxide layer on either side.

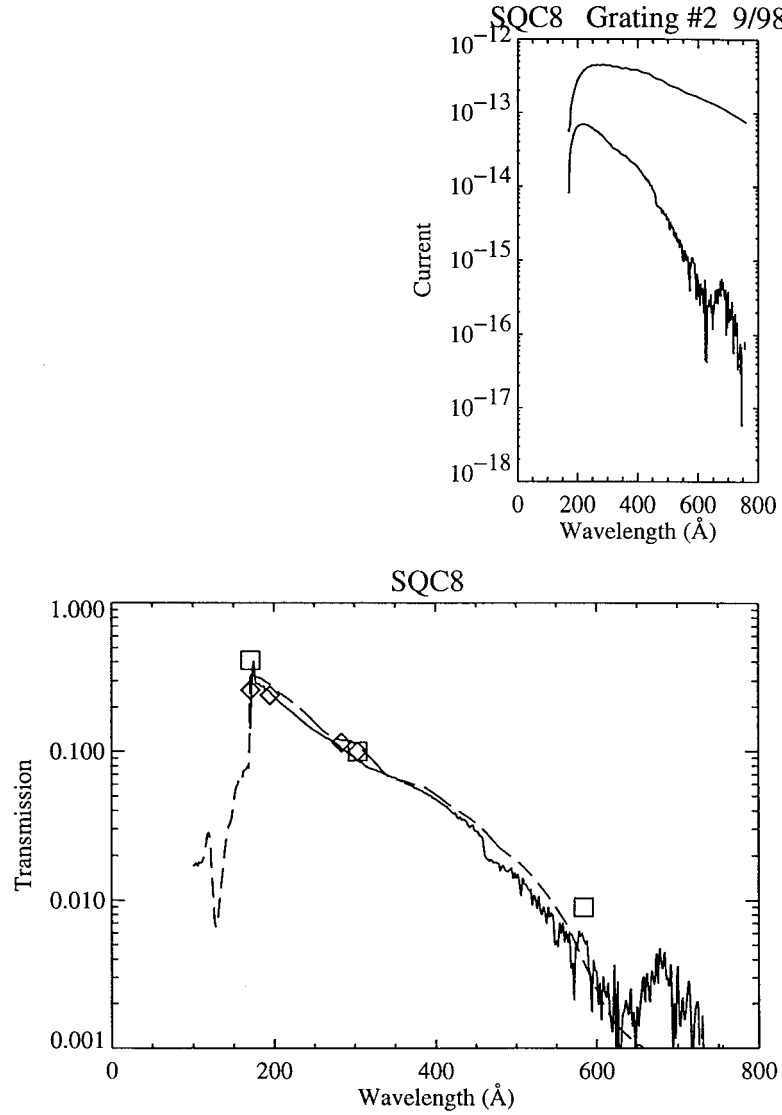


Figure 4. Calibration data for the 'Al+2' filter-wheel filter. *Top right:* are the photodiode currents measured with the filter in and out of the synchrotron beam. *Bottom:* the filter transmission derived from the ratio of the photodiode currents (*solid line*), the in-flight measurements with the 'Al+2' filter on the filterwheel (*diamonds*), measurements performed by PTS (*squares*), measurements of Song (1995) (*triangles*) and a model of the filter (*dashed line*).

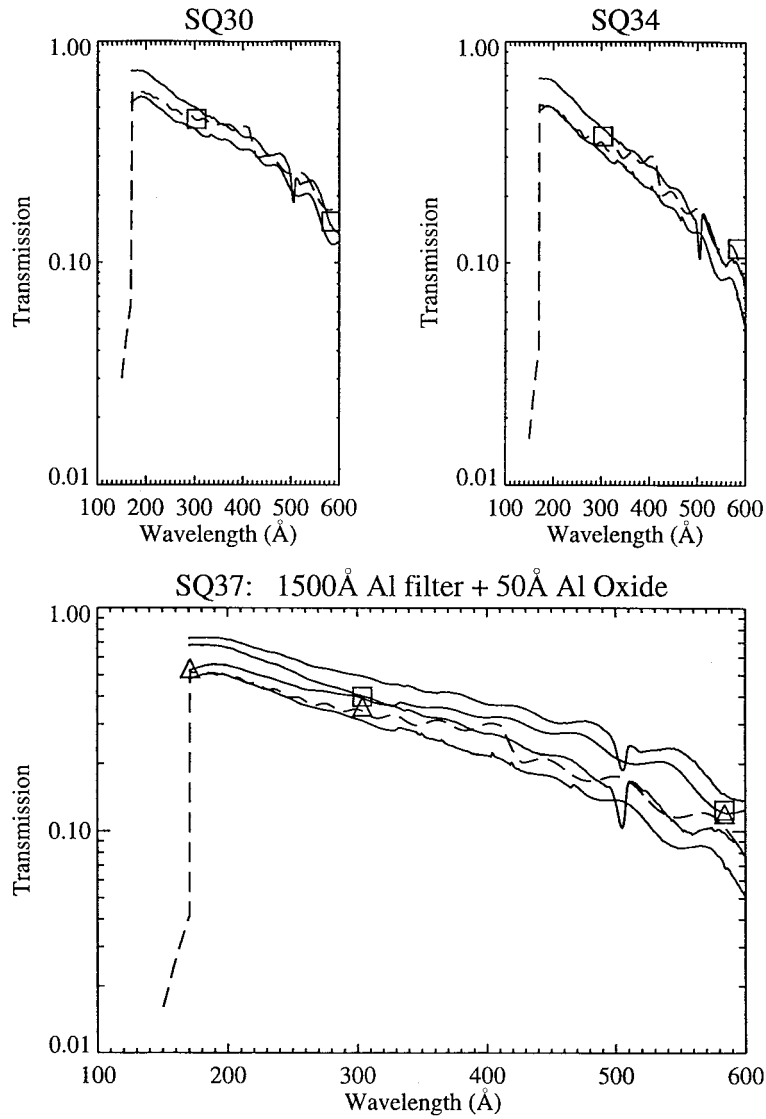


Figure 5. Calibration data for the CCD stray-light filter. *Top left and right* are the transmissions measured for the SQ30 and SQ34 filters which bracket those of the SQ37 CCD stray-light filter. *Bottom*, the filter transmission measured by Song (1995) and PTS together with the SQ30 and SQ34 measurements (*solid lines*) and a model of the filter transmission (*dashed line*).

5. Measurements of the Mirror Reflectivities

The primary and secondary mirrors of the EIT were divided into sectors and specific multilayer coatings applied for the wavelength bands listed in Table I. The mirror reflectivities were measured in November 1993 and in September 1994

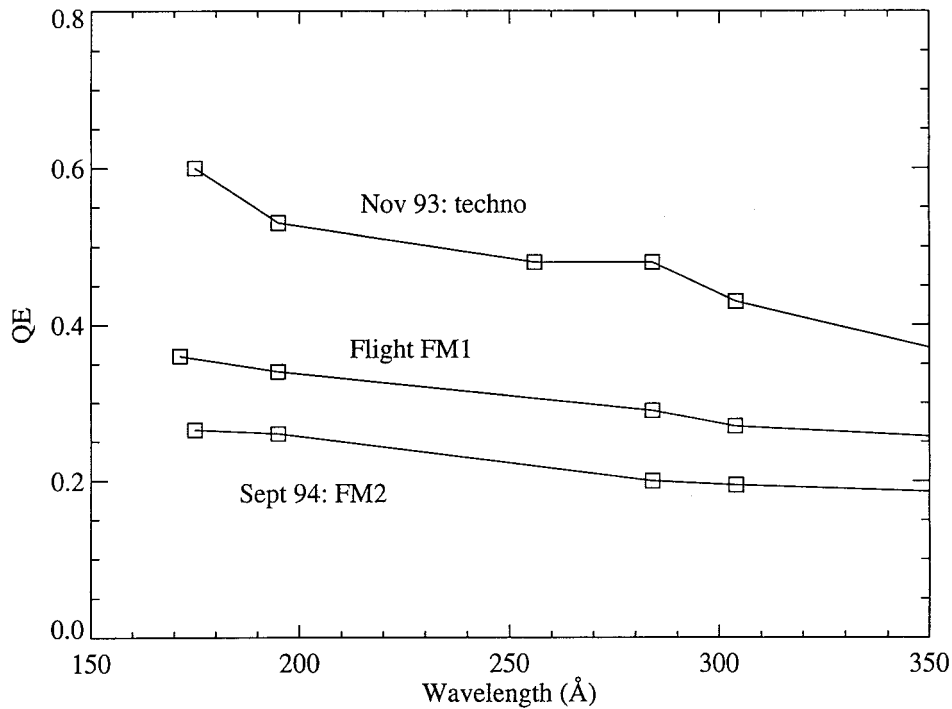


Figure 6. Measurements of the quantum efficiencies of the EIT CCDs used for calibration and in flight.

using the Orsay synchrotron light source. For both series of measurements, the flight mirrors were mounted in the EIT telescope. The beam from the monochromator passed through a small aperture, through the telescope and onto a CCD. A calibrated silicon photodiode was inserted into the beam behind the aperture and in front of the telescope to provide an absolute calibration of the incident radiation. A CCD recorded the number of photons reflected by the primary and secondary mirrors.

In addition, aluminum filters 'D' and 'F' were mounted on opposite sides of the entrance filter wheel which, at that time, could rotate. Measurements of these filters were made and exist but the derived transmission values are, in some cases, puzzling. Some of this uncertainty can probably be traced to errors in the records of the calibration procedures.

Different CCDs and cameras were used for the November 1993 and September 1994 measurements. Further, neither of these units were used in the flight experiment. The quantum efficiencies of these devices were measured and reported by Song (1995). These measurements are shown in Figure 6 together with the measurements of the flight CCD from Delaboudinière *et al.* (1995).

5.1. REFLECTIVITIES OF THE 171 Å MIRRORS

The reflectivities of the 171 Å mirrors were measured during three calibration runs in November 1993 and in September 1994. The measurements of the 171 Å reflectivities below 172 Å made in September 1994 are probably incorrect because of problems with the photodiode amplifier range changes as mentioned earlier. However, photons below 171 Å are highly attenuated by the entrance filters so this is not a significant problem. Above 172 Å, these measurements agree well with those made on 9 November 1993.

For the measurements made on 16 November 1993, the direct flux photodiode files are missing so that data from a different day has been used. This introduces an uncertainty of about a factor of 2. According to the records, the aluminum 'F' filter was in the beam for these measurements and the reflectivities have been corrected for the effect of this filter.

There is a general agreement between the three measurements to within about a factor of 2. We have decided to normalize the three sets of measurements to those obtained in September 1994. This is accomplished by multiplying the 9 November 1993 measurements by a factor of 2.5 and the 16 November 1993 measurements by a factor of 1.6. We have chosen this normalization for the following reasons. In general, the reflectivities of multilayer coatings at 171 Å should be at least as high as those at 195 Å. Our measurements of the 195 Å mirror reflectivities show good internal agreement and indicate a peak combined reflectivity of 0.09. Through our choice of the 171 Å normalization, a similar peak combined reflectivity is derived. The normalized product of the 171 Å primary and secondary mirror reflectivities are shown in Figure 7. The solid line shows our adopted reflectivity as a function of wavelength.

When the multilayer coatings were applied to the EIT mirrors, a set of witness plates, placed nearby, were also coated. Their reflectivities are expected to be similar to those of the EIT mirrors. The reflectivities of these witness plates have been measured (Lemen and Catura, 1996) and the values of the product of the reflectivities of the witness plate reflectivities for the primary and secondary mirrors have also been plotted in Figure 7. The value of the peak reflectivity is close to the value we have measured with the flight mirrors but the peak wavelength for the witness samples is at a longer wavelength.

The peak adopted combined reflectivity of 0.088 shown in Figure 8 is also very close to the product of the peak reflectivities of the primary and secondary mirrors (0.084) measured by Song with the IAS reflectometer (Song, 1995).

5.2. REFLECTIVITIES OF THE 195 Å MIRRORS

The reflectivities of the 195 Å mirrors were measured in five runs in November 1993 and September 1994. The measurements for 10 November 1993 are off-scale and not considered valid. The September 1994 measurements are in relatively good agreement, especially at wavelengths near peak reflectivity. The 11 November 1993

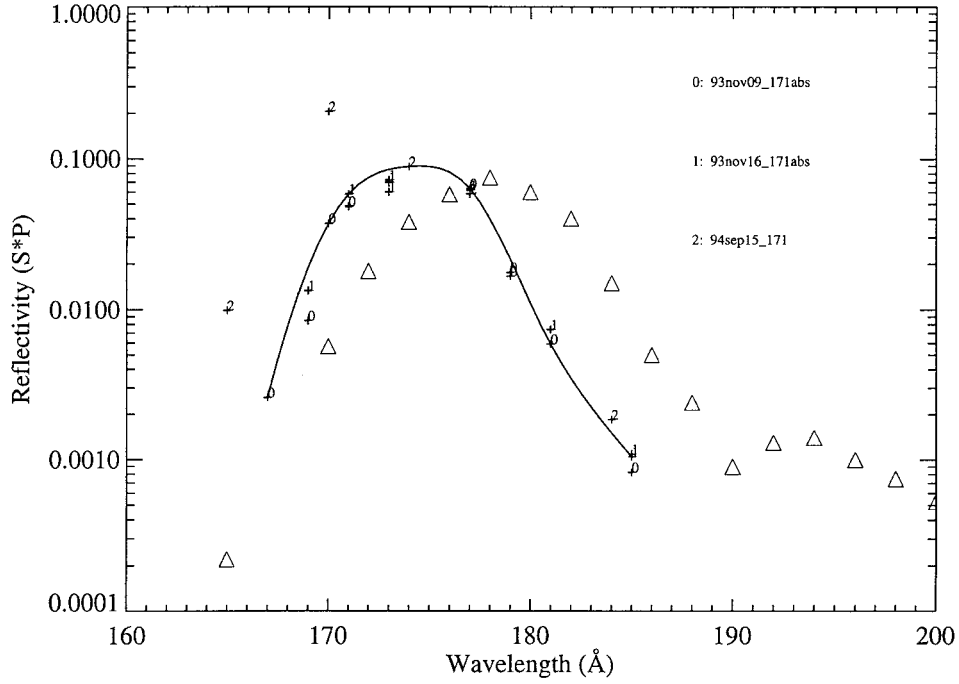


Figure 7. Normalized measured products of the primary and secondary mirror reflectivities for the 171 Å sector. Measurements for the witness plates are plotted as triangles and the adopted values are plotted as a solid line.

measurements indicate a somewhat higher reflectivity than the 1994 September measurements and the 16 November 1993 measurements indicate a somewhat lower reflectivity. To arrive at an adopted set of measurements, we have multiplied the 11 November 1993 measurements by a factor of 0.74 and multiplied the 16 November 1993 measurements by a factor of 1.18. These normalized reflectivities are shown in Figure 8 as a solid line.

The adopted reflectivities, derived from the geometrical average of the November 1993 and September 1994 measurements, are shown in Figure 8. The normalized measurements have a higher peak reflectivity than that of the witness mirrors and peak at a shorter wavelength. The peak combined reflectivity of 0.090 shown in Figure 8 is also somewhat higher than the product of the peak reflectivities of the primary and secondary mirrors (0.059) measured by Song with the IAS reflectometer (Song, 1995).

5.3. REFLECTIVITIES OF THE 284 Å MIRRORS

The reflectivities of the 284 Å mirrors were measured in seven runs. One set of measurement obtained on 11 November 1993 differ drastically from the others and are not included here. The remaining measurements generally agree to within a

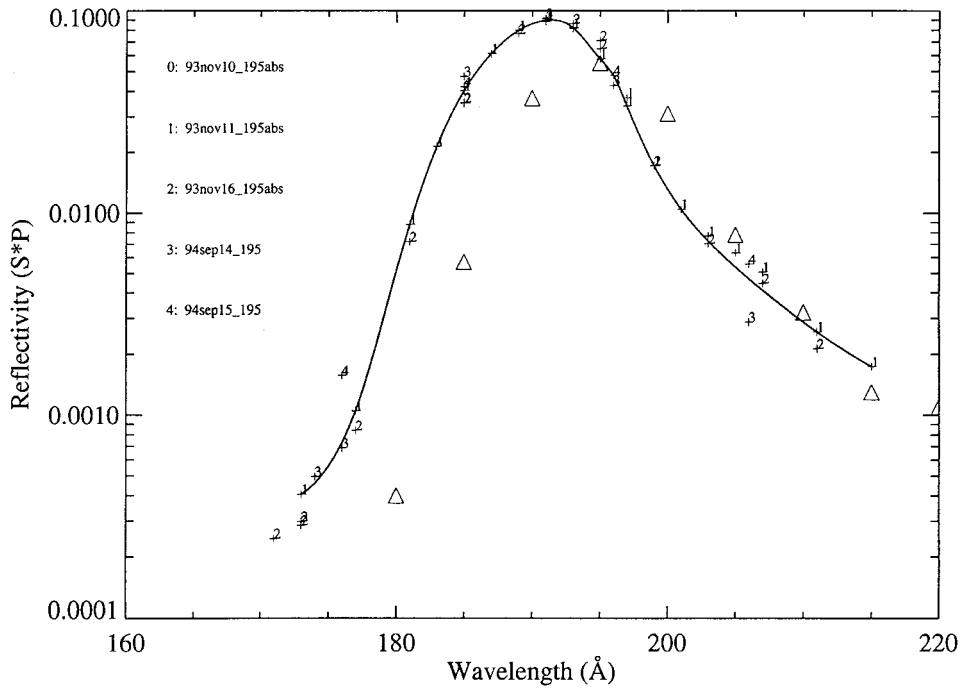


Figure 8. Normalized measured products of the primary and secondary mirror reflectivities for the 195 Å sector. Measurements for the witness plates are plotted as triangles and the adopted values are plotted as a solid line.

factor of 2. The measurements from 17 and 18 November 1993 are in good agreement as are the three sets of measurements made in September 1994. However, these two groups are separated by a factor of about 1.8. To bring the various sets of measurements into agreement, we have used the geometric mean of six measurement sets, excluding the data from 11 November 1993. This results in the measurements from 17 and 18 November 1993 being multiplied by a factor of 1.26, the measurements from 16 November 1993 being multiplied by a factor of 1.8, and the 1994 September measurements being multiplied by a factor of 0.70. These normalized measurements and the adopted final reflectivity values are shown in Figure 9.

These measurements give a reflectivity roughly an order of magnitude higher than that of the witness mirrors. The peak combined reflectivity of 0.030 shown in Figure 9 is also somewhat higher than the product of the peak reflectivities of the primary and secondary mirrors (0.018) measured by Song with the IAS reflectometer (Song, 1995).

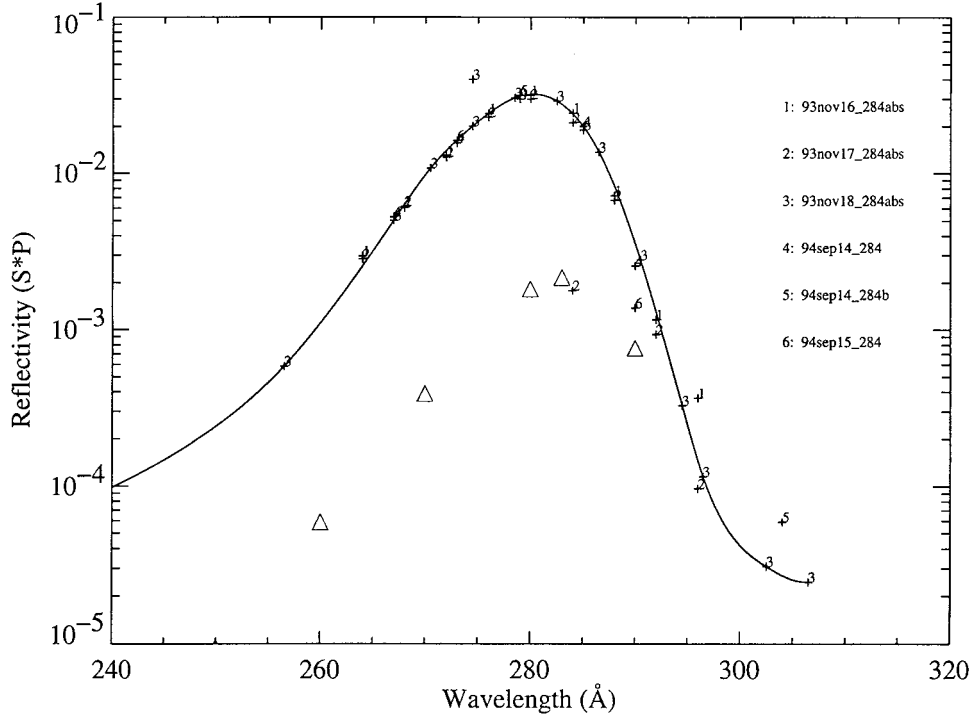


Figure 9. Normalized measured products of the primary and secondary mirror reflectivities for the 284 Å sector. Measurements for the witness plates are plotted as triangles and the adopted values are plotted as a solid line.

5.4. REFLECTIVITIES OF THE 304 Å MIRRORS

The reflectivities of the 304 Å mirrors were measured in 6 runs and the results are shown in Figure 10. One set of measurement obtained on 9 November 1993 differ drastically from those shown and are not included here. The remaining measurements generally agree to within a factor of 2.5. The measurements from 10 and 16 November 1993 are in good agreement as are the two sets of measurements made on 17 November 1993. However, the two sets generally differ by about a factor of 2. The single set of measurements from September 1994 are a factor of 2 higher than any of the 1993 November measurements. To bring the various sets of measurements into agreement, we have used the geometric mean of the measurements from 10, 16, 17 November 1993 (both sets). This results in the measurements from 10 and 16 November 1993 being multiplied by a factor of 1.4, the measurements from 17 November 1993 being multiplied by a factor of 0.64, the second set of measurements from 17 November 1993 being multiplied by a factor of 0.80 and the 1994 September measurements being multiplied by a factor of 0.36. These normalized measurements and the adopted final reflectivity values are shown in Figure 10.

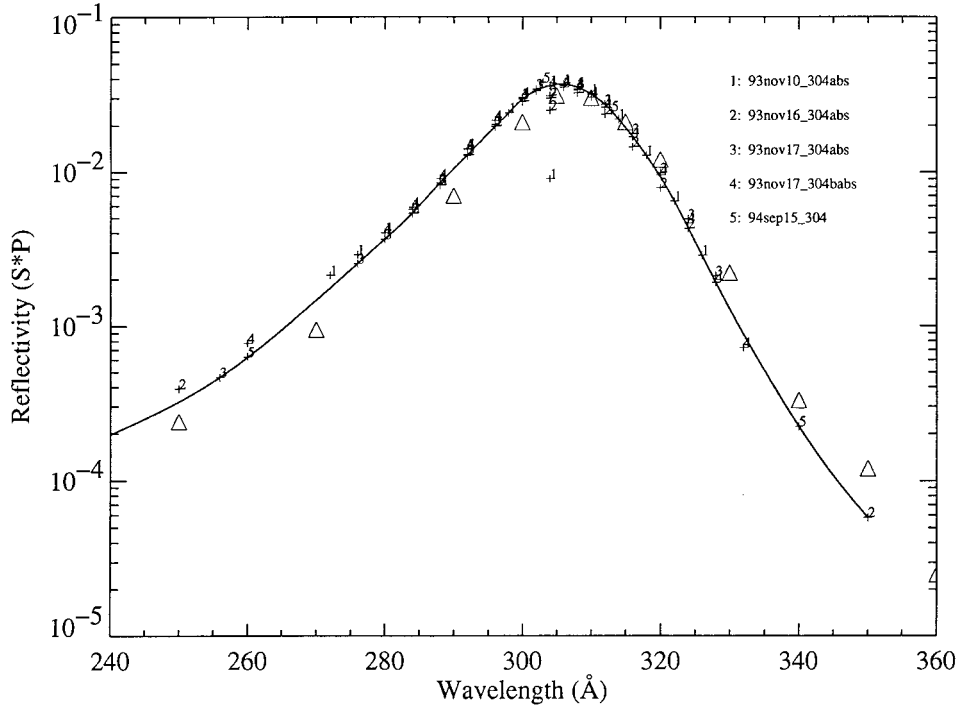


Figure 10. Normalized measured products of the primary and secondary mirror reflectivities for the 304 Å sector. Measurements for the witness plates are plotted as triangles and the adopted values are plotted as a solid line.

These measurements give a reflectivity very close to that of the witness mirrors. The peak combined reflectivity of 0.037 shown in Figure 10 is comparable to the product of the peak reflectivities of the primary and secondary mirrors (0.033) measured by Song with the IAS reflectometer (Song, 1995).

6. Measurements of the CCD and Camera Response

The calibration of the CCD is stated in terms of an efficiency ϵ which is defined by

$$q = \epsilon \frac{h\nu}{3.65 \text{ eV}} Ft, \quad (1)$$

where q is the charge collected from the CCD, F is the flux incident on the CCD in photons s^{-1} , and t the exposure time. It is assumed that at EUV wavelengths an electron-hole pair is created for each 3.65 eV of photon energy $h\nu$. ϵ is basically the ratio of electrons collected to electrons created. A loss of efficiency is created by the fact that not all electrons migrate to the potential wells.

Measurements of the quantum efficiency of the CCD detector have been reported by Song (1995) at 171, 195, 284, and 304 Å. These are the same values

TABLE IV
EIT CCD quantum efficiency

Wavelength	Efficiency ϵ
171 Å	0.36
195 Å	0.34
284 Å	0.29
304 Å	0.27
550 Å	0.20
800 Å	0.02

reported by Delaboudinière *et al.* (1995) and, for completeness, are shown in Table IV and plotted in Figure 6. We will simply use a linear interpolation of these measurements. The CCD amplifier output was set so that 1 DN (the output value) was produced for 16.7 electrons collected at the output register. This value is derived from analyses of photon transfer using in-flight calibration lamp exposures.

7. Error Budget

7.1. ALUMINUM/CELLULOID FILTERS

Aluminum/celluloid filters are used as entrance filters for all of the sectors. For the 171 Å sector entrance filters (I1 and I2) the two sets of measurements agree to within about 20%. For the 284 Å sector entrance filters (A1 and A2) the two sets of measurements agree to within about 25%. For the 304 Å sector entrance filters (O1 and O2) the two sets of measurements agree to within about 5%. For the 195 Å sector entrance filters (L1 and L2) there is only a single set of measurements so an accuracy of about 25% should be assigned to these values.

For the ‘A1+2’ aluminum/celluloid filter on the filterwheel, only a single set of synchrotron measurements exists. These measurements agree to within about 15–20% with the transmissions derived from in-flight data so it should be reasonable to assign an accuracy of 15–20% to the error in the transmission of this filter.

These comparisons suggest that, in general, the transmissions of the aluminum/celluloid filters is known to an accuracy of about 25%.

7.2. PURE ALUMINUM FILTERS

The CCD stray-light filter (SQ30) was apparently measured at the synchrotron but only those reflectivity values at 171, 304, and 584 Å still remain. Measurements at 304 and 584 Å by PTS are also available. Measurements of the SQ30 and SQ34

aluminum filters revealed an agreement between the measurements with different gratings at about the 30% level so that an error of about 30% can be assigned to the calibration of the CCD stray-light filter.

For the filter-wheel filter ‘A1+1’ (SQ35), preflight measurements were made only at 304 and 584 Å by PTS. The only other measurements are those made in flight. At 304 Å there is agreement between these and the PTS measurements. The derived model filter seems to reproduce the in-flight values at about the 10% level which is our adopted calibration error for the CCD stray-light filter.

7.3. MIRROR REFLECTIVITIES

For the 171 Å sector at wavelengths above 170 Å, there is a spread of about a factor of 2.5 between the three sets of measurement. These measurements have been normalized to the set of measurements that provide the highest reflectivity. Consequently, we estimate that the error budget for the product of the reflectivities of the primary and secondary mirrors is about a factor of 2.5.

For the 195 Å sector, the measurements indicate a total spread of about a factor of 1.6 between various values. The adopted values have been arrived at by taking a geometric mean so that the variation about the mean value is a factor of 1.3. Consequently, an error of 30% can be assigned to 195 Å sector reflectivity measurements.

For the 284 Å sector, the measurements indicate a total spread of about a factor of 2.5 between various values. The adopted values have been arrived at by taking a geometric mean so that the variation about the mean value is a factor of 1.4. Consequently, an error of 40% can be assigned to the 284 Å sector reflectivity measurements.

For the 304 Å sector, the measurements indicate a total spread of about a factor of 2.2 between various values. The adopted values have been arrived at by taking a geometric mean so that the variation about the mean value is a factor of 1.4. Consequently, an error of 40% can be assigned to the 304 Å sector reflectivity measurements.

7.4. CCD

Song (1995) reports 3 sets of measurements of the EIT flight CCD quantum efficiency. There variations between the two sets range from a factor of about 1.2 at 170 Å to a factor of about 1.5 at 304 Å.

7.5. TOTAL CALIBRATION ERROR BUDGET

The net effect of the likely errors in the calibration of the various optical elements is shown in Table V. For the filterwheel uncertainties, we have use the values assigned to the ‘A1+1’ filter.

TABLE V
Net EIT calibration error budget

Element	Sector			
	171 Å (%)	195 Å (%)	284 Å (%)	304 Å (%)
Entrance filter	25	25	25	25
Mirrors	150	30	40	40
Filter wheel	10	10	10	10
Stray-light filter	30	30	30	30
CCD	20	30	40	50
Total	150	60	70	75

8. Total EIT Throughput and Coronal Response

The digital output for the EIT is given in terms of a count rate CR in $\text{DN s}^{-1} \text{ pixel}^{-1}$:

$$CR = \frac{A a_{\text{pix}}}{d} \int \frac{T_{\text{EF}} R_{\text{SM}} R_{\text{PM}} T_{\text{FW}} T_{\text{SL}}}{f^2} \frac{12398}{3.65\lambda} \epsilon P(\lambda) d\lambda, \quad (2)$$

where A is the open aperture area, a_{pix} is the area of a CCD pixel, d is the digitization constant (16.7 electrons per DN), T_{EF} is the transmission of the entrance filter, T_{FW} is the transmission of the filter-wheel filter, T_{SL} is the transmission of the CCD stray-light filter, R_{PM} is the reflectivity of the primary mirror, R_{SM} is the reflectivity of the secondary mirror, λ is the wavelength in Å, f is the telescope focal length, ϵ is the quantum efficient of the CCD, and $P(\lambda)$ is the incident flux in $\text{photons cm}^{-2} \text{ s}^{-1} \text{ sr}^{-1} \text{ Å}^{-1}$. Except for A , a_{pix} , f and d , all variables in this equation are functions of wavelength λ .

In order to compare the throughput of the EIT with other instruments, it is useful to calculate the effective area,

$$A_{\text{eff}} = A T_{\text{EF}} R_{\text{PM}} R_{\text{SM}} T_{\text{FW}} T_{\text{SL}} \epsilon. \quad (3)$$

The effective area A_{eff} for each of the 4 wavelength sectors and for the various filter-wheel positions are presented in Tables VI–IX and plotted in Figure 11.

The transition region and coronal emissions that are detected by the EIT are created by the electron collisional excitation of ionized species present in solar plasmas. In addition, there is a contribution to the spectrum from continuum emission. The distribution of electron velocities follows a Maxwell–Boltzmann distribution so that the emergent spectrum is determined largely by the amount of plasma along the line of sight and the temperature of that plasma. P can then be expressed as

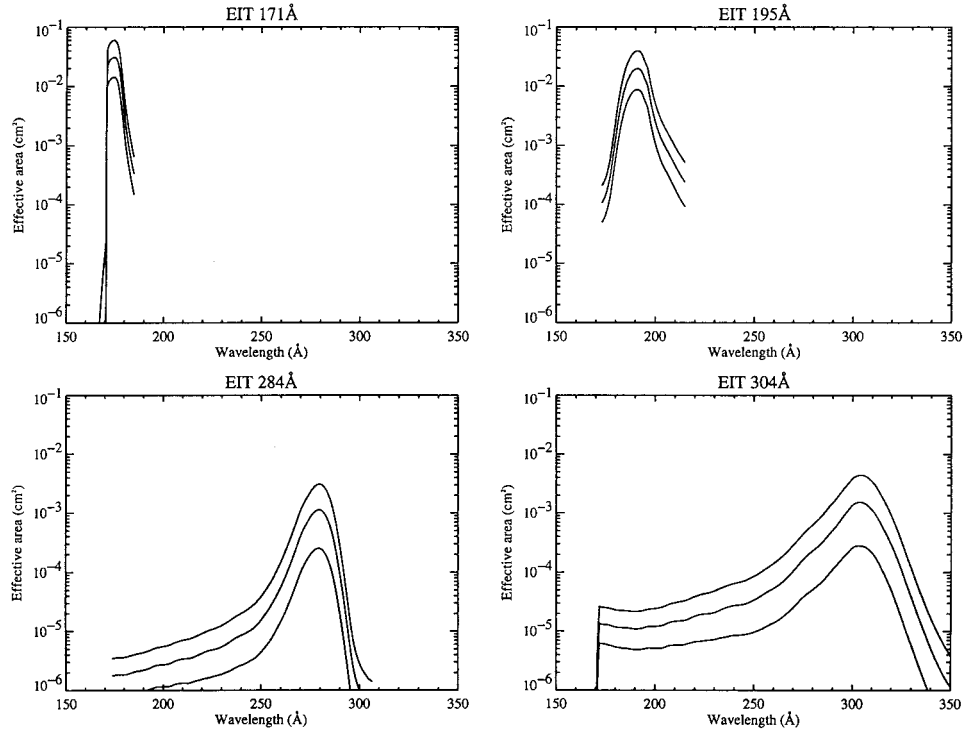


Figure 11. The effective area for the various EIT sector and filter-wheel combinations.

TABLE VI
Effective area A_{eff} (cm^2) of the EIT 171 Å band

Wavelength (Å)	Al+1	Al+2	Clear
168	9.07e-08	9.17e-10	2.44e-06
170	5.92e-07	6.53e-09	1.46e-05
172	2.64e-02	1.21e-02	5.13e-02
174	3.03e-02	1.42e-02	5.92e-02
176	2.81e-02	1.29e-02	5.45e-02
178	1.35e-02	6.10e-03	2.62e-02
180	3.60e-03	1.65e-03	7.07e-03
182	1.11e-03	5.07e-04	2.19e-03
184	4.78e-04	2.13e-04	9.38e-04
186	2.63e-03	9.00e-04	4.93e-03

TABLE VII
Effective area A_{eff} (cm^2) of the EIT 195 Å band

Wavelength (Å)	Al+1	Al+2	Clear
175	1.46e-04	6.78e-05	2.85e-04
180	1.27e-03	5.85e-04	2.51e-03
185	9.69e-03	4.32e-03	1.90e-02
190	1.93e-02	8.63e-03	3.84e-02
195	1.25e-02	5.38e-03	2.46e-02
200	2.54e-03	1.08e-03	5.13e-03
205	9.48e-04	3.89e-04	1.95e-03
210	4.60e-04	1.81e-04	9.52e-04
215	2.39e-04	9.27e-05	5.17e-04

$$P(\lambda, n_e, T) = \int G(n_e, T, \lambda) \text{DEM}(T) dT ; \quad (4)$$

G is the theoretical emissivity of coronal plasmas in photons $\text{cm}^{-6} \text{s}^{-1} \text{sr}^{-1} \text{Å}^{-1}$ which is an explicit function of the density n_e and temperature T of the solar plasma described by the differential emission measure $\text{DEM}(T)$ in cm^{-5} . The CHIANTI database (Dere *et al.*, 1997) is an excellent package for calculating the function $G(n_e, T, \lambda)$ for spectral line emission from coronal plasmas. The free-free continuum emission has been calculated using the free-free gaunt factors of Sutherland (1998). For the free-bound emission, a gaunt factor of unity has been used. The EIT count rate CR can be expressed as

$$CR = \frac{a_{\text{pix}}}{d} \int \frac{A_{\text{eff}}(\lambda)}{f^2} \frac{12398}{3.65\lambda} \int G(n_e, T, \lambda) \text{DEM}(T) dT d\lambda . \quad (5)$$

For a broadband instrument like the EIT, the function G only weakly depends on the electron density n_e . If we assume that the electron density is a function only of temperature or a constant, then we can write this as

$$CR = \int H(T) \text{DEM}(T) dT , \quad (6)$$

where

$$H(T) = \frac{a_{\text{pix}}}{d} \int \frac{A_{\text{eff}}(\lambda)}{f^2} \frac{12398}{3.65\lambda} G(n_e(T), T, \lambda) d\lambda \quad (7)$$

and, in a one-dimensional representation,

$$\text{DEM}(T) = \int_T^{T+dT} n_e n_H dh , \quad (8)$$

TABLE VIII
Effective area A_{eff} (cm^2) of the EIT 284 Å band

Wavelength (Å)	Al+1	Al+2	Clear
175	1.80e−06	8.32e−07	3.50e−06
180	1.84e−06	8.43e−07	3.60e−06
185	2.03e−06	9.07e−07	3.98e−06
190	2.19e−06	9.81e−07	4.36e−06
195	2.53e−06	1.09e−06	5.00e−06
200	2.71e−06	1.15e−06	5.50e−06
205	3.00e−06	1.23e−06	6.16e−06
210	3.39e−06	1.33e−06	7.03e−06
215	3.56e−06	1.38e−06	7.71e−06
220	4.21e−06	1.54e−06	9.12e−06
225	4.81e−06	1.68e−06	1.07e−05
230	5.41e−06	1.87e−06	1.25e−05
235	6.86e−06	2.19e−06	1.59e−05
240	8.53e−06	2.64e−06	2.02e−05
245	1.05e−05	3.18e−06	2.60e−05
250	1.54e−05	4.38e−06	3.89e−05
255	2.72e−05	7.18e−06	6.87e−05
260	5.56e−05	1.44e−05	1.46e−04
265	1.37e−04	3.48e−05	3.74e−04
270	3.97e−04	9.54e−05	1.08e−03
275	8.39e−04	1.95e−04	2.25e−03
280	1.12e−03	2.48e−04	3.07e−03
285	5.81e−04	1.27e−04	1.67e−03
290	9.20e−05	2.00e−05	2.68e−04
295	6.14e−06	1.25e−06	1.77e−05
300	9.90e−07	1.87e−07	2.82e−06
305	5.22e−07	9.51e−08	1.53e−06

where n_H is the proton density and h is the distance along the observer's line of sight.

We have used the CHIANTI database to calculate P and integrate it over the effective area to derive the plasma response functions H which are plotted in Figure 12 and listed in Tables X–XIII. For these calculations, we have used the coronal elemental abundances of Meyer (1985) and the ionization equilibrium calculations of Arnaud and Rothenflug (1985) and those of Arnaud and Raymond (1992) for

TABLE IX
Effective area A_{eff} (cm^2) of the EIT 304 Å band

Wavelength (Å)	Al+1	Al+2	Clear
150	2.30e-11	6.71e-14	1.47e-09
155	5.72e-11	2.44e-13	2.81e-09
160	1.40e-10	8.56e-13	5.32e-09
165	3.08e-10	2.61e-12	9.37e-09
170	2.99e-09	3.29e-11	7.38e-08
175	1.30e-05	6.02e-06	2.53e-05
180	1.18e-05	5.41e-06	2.31e-05
185	1.14e-05	5.09e-06	2.23e-05
190	1.09e-05	4.88e-06	2.17e-05
195	1.16e-05	5.01e-06	2.29e-05
200	1.20e-05	5.11e-06	2.44e-05
205	1.30e-05	5.34e-06	2.68e-05
210	1.47e-05	5.79e-06	3.05e-05
215	1.53e-05	5.93e-06	3.31e-05
220	1.80e-05	6.58e-06	3.89e-05
225	1.97e-05	6.89e-06	4.37e-05
230	2.08e-05	7.22e-06	4.82e-05
235	2.46e-05	7.86e-06	5.69e-05
240	2.74e-05	8.49e-06	6.49e-05
245	2.89e-05	8.77e-06	7.18e-05
250	3.41e-05	9.66e-06	8.59e-05
255	4.30e-05	1.14e-05	1.09e-04
260	5.37e-05	1.40e-05	1.41e-04
265	7.11e-05	1.80e-05	1.94e-04
270	1.05e-04	2.53e-05	2.86e-04
275	1.64e-04	3.81e-05	4.40e-04
280	2.32e-04	5.15e-05	6.38e-04
285	3.29e-04	7.16e-05	9.43e-04
290	5.14e-04	1.12e-04	1.50e-03
295	8.54e-04	1.74e-04	2.46e-03
300	1.38e-03	2.61e-04	3.93e-03
305	1.52e-03	2.76e-04	4.44e-03
310	1.12e-03	2.11e-04	3.43e-03
315	6.10e-04	1.12e-04	1.91e-03
320	2.84e-04	4.87e-05	8.80e-04
325	1.09e-04	1.71e-05	3.31e-04

TABLE IX
continued.

Wavelength (Å)	Al+1	Al+2	Clear
330	3.77e-05	5.74e-06	1.15e-04
335	1.33e-05	2.04e-06	4.18e-05
340	4.99e-06	7.61e-07	1.64e-05
345	2.17e-06	3.23e-07	7.30e-06
350	1.14e-06	1.59e-07	3.81e-06

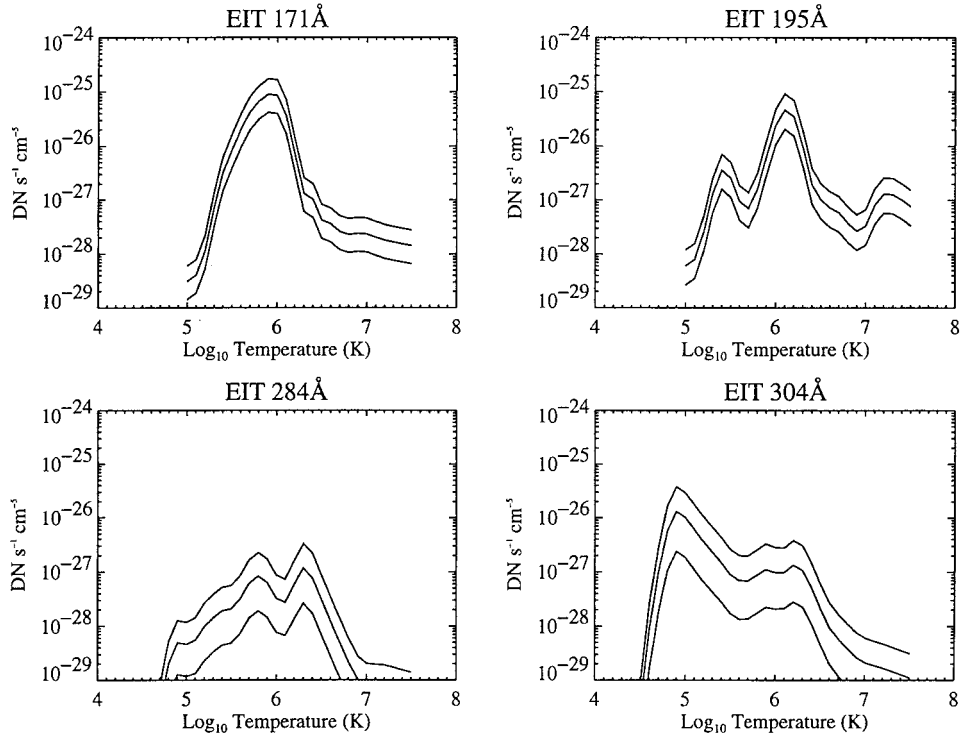


Figure 12. EIT plasma response $H(T)$ for various sector and filter-wheel combinations. In each plot, the top curve includes the clear filter-wheel filter, the middle curve the 'Al+1' filter and the bottom curve the 'Al+2' filter.

the ionization equilibrium of iron. We have assumed a constant electron pressure $N_e T = 6 \times 10^{15} \text{ cm}^{-3} \text{ K}$.

The reflectivities of the 171 Å wavelength sector peaks at around 175 Å. Its response is dominated at coronal temperatures by the strong Fe IX line at 171.1 Å and the strong Fe X lines at 174.5 Å and 177.2 Å. There is a weak transition region

TABLE X

Plasma response $H(T)$ ($\text{DN s}^{-1} \text{ cm}^{-5}$) for the EIT
171 Å band

$\text{Log}_{10} T$ (K)	Al+1	Al+2	Clear
5.0	3.06e-29	1.41e-29	5.96e-29
5.1	4.04e-29	1.86e-29	7.87e-29
5.2	1.14e-28	5.24e-29	2.21e-28
5.3	7.07e-28	3.26e-28	1.37e-27
5.4	3.29e-27	1.52e-27	6.39e-27
5.5	8.43e-27	3.91e-27	1.63e-26
5.6	2.05e-26	9.53e-27	3.94e-26
5.7	4.26e-26	1.98e-26	8.19e-26
5.8	6.70e-26	3.11e-26	1.29e-25
5.9	8.95e-26	4.15e-26	1.73e-25
6.0	8.48e-26	3.93e-26	1.64e-25
6.1	3.69e-26	1.71e-26	7.17e-26
6.2	7.03e-27	3.24e-27	1.37e-26
6.3	1.32e-27	6.04e-28	2.56e-27
6.4	1.03e-27	4.69e-28	1.99e-27
6.5	4.22e-28	1.94e-28	8.21e-28
6.6	3.60e-28	1.65e-28	7.01e-28
6.7	2.58e-28	1.19e-28	5.03e-28
6.8	2.29e-28	1.05e-28	4.45e-28
6.9	2.41e-28	1.11e-28	4.69e-28
7.0	2.34e-28	1.08e-28	4.55e-28
7.1	2.03e-28	9.36e-29	3.96e-28
7.2	1.80e-28	8.29e-29	3.51e-28
7.3	1.65e-28	7.62e-29	3.22e-28
7.4	1.54e-28	7.08e-29	3.00e-28
7.5	1.43e-28	6.58e-29	2.79e-28

component from O V ($2s^2 - 2s3p$) and O VI ($2p - 3d$) transitions. In a flare, the response is primarily due to continuum emission at 10^7K .

The reflectivities of the 195 Å wavelength sector peaks at around 191 Å. In the quiet Sun, the response will be dominated by the Fe XI lines at 188.2 Å and the Fe XII lines at 192.4, 193.5, and 195.1 Å. There is a weak transition region component from O V $2s2p - 2s3d$ transitions. In flares, there is a significant contribution from Fe XXIV at 192.0 Å.

TABLE XI

Plasma response $H(T)$ ($\text{DN s}^{-1} \text{ cm}^{-5}$) for the EIT 195 Å band

$\text{Log}_{10} T \text{ (K)}$	Al+1	Al+2	Clear
5.0	6.01e-29	2.64e-29	1.19e-28
5.1	7.97e-29	3.49e-29	1.58e-28
5.2	2.57e-28	1.13e-28	4.92e-28
5.3	1.32e-27	5.81e-28	2.55e-27
5.4	3.56e-27	1.57e-27	7.03e-27
5.5	2.53e-27	1.12e-27	4.98e-27
5.6	9.42e-28	4.17e-28	1.84e-27
5.7	6.92e-28	3.07e-28	1.36e-27
5.8	1.55e-27	6.90e-28	3.06e-27
5.9	6.32e-27	2.81e-27	1.25e-26
6.0	2.38e-26	1.06e-26	4.71e-26
6.1	4.62e-26	2.03e-26	9.16e-26
6.2	3.49e-26	1.53e-26	6.94e-26
6.3	9.53e-27	4.15e-27	1.90e-26
6.4	1.91e-27	8.36e-28	3.80e-27
6.5	1.00e-27	4.41e-28	1.99e-27
6.6	7.17e-28	3.16e-28	1.42e-27
6.7	5.85e-28	2.58e-28	1.16e-27
6.8	3.75e-28	1.65e-28	7.45e-28
6.9	2.68e-28	1.18e-28	5.33e-28
7.0	3.34e-28	1.48e-28	6.65e-28
7.1	8.04e-28	3.56e-28	1.60e-27
7.2	1.29e-27	5.70e-28	2.57e-27
7.3	1.26e-27	5.56e-28	2.51e-27
7.4	1.00e-27	4.44e-28	2.01e-27
7.5	7.59e-28	3.36e-28	1.52e-27

The reflectivities of the 284 Å wavelength sector peaks at around 280 Å. The dominant contributor to the EIT response in this wavelength sector is the Fe xv line at 284.1 Å at a temperature near 2×10^6 K. However, there are a number of Mg VII, Si VII, and Si VIII lines near the peak of the bandpass that provide a response around 6×10^5 K.

The reflectivities of the 304 Å wavelength sector peaks at around 306 Å. The dominant contributor to the EIT is from the He II $1s - 2p$ doublet at 304 Å. Weaker contributors such as Si IX 296 Å, Si XI 303 Å and Mg VIII 311 Å provide a response

TABLE XII
 Plasma response $H(T)$ ($\text{DN s}^{-1} \text{ cm}^{-5}$) for the EIT
 284 Å band

$\text{Log}_{10} T \text{ (K)}$	Al+1	Al+2	Clear
4.7	2.99e-30	7.59e-31	7.73e-30
4.8	1.98e-29	5.05e-30	5.10e-29
4.9	4.91e-29	1.26e-29	1.26e-28
5.0	4.61e-29	1.17e-29	1.18e-28
5.1	5.48e-29	1.32e-29	1.43e-28
5.2	9.70e-29	2.26e-29	2.62e-28
5.3	1.42e-28	3.31e-29	3.83e-28
5.4	1.91e-28	4.45e-29	5.14e-28
5.5	2.07e-28	4.83e-29	5.58e-28
5.6	3.13e-28	7.28e-29	8.46e-28
5.7	6.14e-28	1.41e-28	1.66e-27
5.8	8.28e-28	1.90e-28	2.24e-27
5.9	6.31e-28	1.45e-28	1.70e-27
6.0	3.22e-28	7.64e-29	8.65e-28
6.1	2.72e-28	6.70e-29	7.27e-28
6.2	5.76e-28	1.35e-28	1.58e-27
6.3	1.17e-27	2.63e-28	3.30e-27
6.4	7.74e-28	1.71e-28	2.19e-27
6.5	3.14e-28	6.94e-29	8.90e-28
6.6	1.24e-28	2.76e-29	3.52e-28
6.7	5.06e-29	1.13e-29	1.42e-28
6.8	2.14e-29	4.86e-30	5.96e-29
6.9	1.02e-29	2.37e-30	2.81e-29
7.0	7.37e-30	1.73e-30	2.01e-29
7.1	7.17e-30	1.71e-30	1.94e-29
7.2	7.00e-30	1.69e-30	1.89e-29
7.3	6.39e-30	1.54e-30	1.72e-29
7.4	5.72e-30	1.37e-30	1.54e-29
7.5	5.15e-30	1.23e-30	1.39e-29

TABLE XIII

Plasma response $H(T)$ ($\text{DN s}^{-1} \text{ cm}^{-5}$) for the EIT
304 Å band

$\text{Log}_{10} T \text{ (K)}$	Al+1	Al+2	Clear
4.5	3.02e-30	5.53e-31	8.76e-30
4.6	8.59e-29	1.57e-29	2.49e-28
4.7	9.59e-28	1.76e-28	2.78e-27
4.8	5.76e-27	1.05e-27	1.67e-26
4.9	1.30e-26	2.38e-27	3.77e-26
5.0	1.02e-26	1.86e-27	2.95e-26
5.1	6.02e-27	1.10e-27	1.74e-26
5.2	3.62e-27	6.65e-28	1.05e-26
5.3	2.32e-27	4.30e-28	6.71e-27
5.4	1.48e-27	2.78e-28	4.28e-27
5.5	9.04e-28	1.72e-28	2.61e-27
5.6	6.95e-28	1.35e-28	2.01e-27
5.7	6.84e-28	1.36e-28	1.98e-27
5.8	8.71e-28	1.74e-28	2.55e-27
5.9	1.11e-27	2.23e-28	3.30e-27
6.0	9.82e-28	2.08e-28	2.84e-27
6.1	9.87e-28	2.14e-28	2.78e-27
6.2	1.34e-27	2.78e-28	3.80e-27
6.3	1.08e-27	2.27e-28	3.07e-27
6.4	5.15e-28	1.10e-28	1.47e-27
6.5	2.08e-28	4.44e-29	5.93e-28
6.6	9.42e-29	2.00e-29	2.70e-28
6.7	5.82e-29	1.20e-29	1.67e-28
6.8	3.88e-29	7.81e-30	1.11e-28
6.9	2.68e-29	5.37e-30	7.70e-29
7.0	2.12e-29	4.31e-30	6.08e-29
7.1	1.87e-29	3.94e-30	5.32e-29
7.2	1.68e-29	3.67e-30	4.73e-29
7.3	1.47e-29	3.23e-30	4.11e-29
7.4	1.27e-29	2.78e-30	3.56e-29
7.5	1.10e-29	2.40e-30	3.11e-29

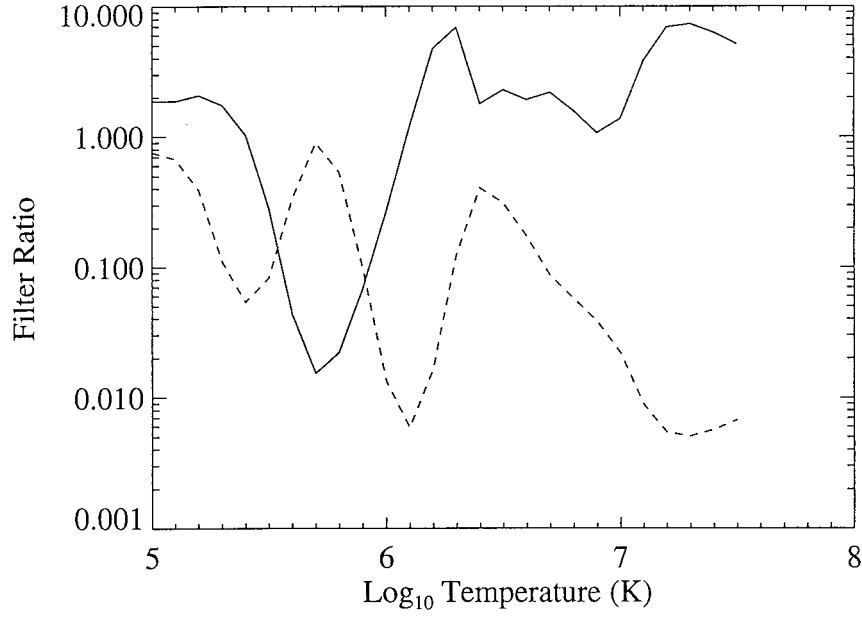


Figure 13. The ratios of the EIT wavelength sectors as a function of temperature for the ‘Al+I’ filter-wheel position. The ratio 195/171 is the *solid line* and the ratio 284/195 is the *dashed line*.

in the 8×10^5 to 3×10^6 K range. Although this response is relatively weak compared to that at 10^5 K, the emission measure at 10^6 is usually significantly greater than that at 10^5 K.

Ratios of the intensities observed in the EIT coronal bands (171, 195 and 284 Å) can be used as temperature diagnostics (Moses, 1997). We have calculated these ratios for the various filterwheel positions and these values are shown in Table XIV. In addition, a plot of the ratios for the ‘Al+I’ filter is shown in Figure 13. Clearly, the ratio technique is valid only over a limited range of temperatures, from 5×10^5 K to 2×10^6 K for the 195/171 ratio and from 1.3×10^6 K to 2.5×10^6 K for the 284/195 ratio.

9. Comparison with Observations

The calibration derived from the synchrotron measurements can be checked by comparing expected count rates with predicted count rates based on our knowledge of the structure of the solar atmosphere as specified by the differential emission measure (DEM). For the observations, we have selected two periods when observations were made through all the relevant filter-wheel combinations. The first period is between 21 February and 1 March 1996 when the Sun was very quiet and the only active region was extremely small. The second period was on 5 November 1998, shortly after SOHO was recovered from an extended period when it was

TABLE XIV
Ratios of various EIT wavelength sectors as a function of temperature

$\text{Log}_{10} T \text{ (K)}$	195/171			284/195		
	Clear	Al+1	Al+2	Clear	Al+1	Al+2
5.0	2.00	1.96	1.87	0.9861	0.7567	0.4383
5.1	2.00	1.96	1.87	0.9073	0.6743	0.3709
5.2	2.22	2.17	2.07	0.5329	0.3893	0.2064
5.3	1.86	1.81	1.73	0.1500	0.1102	0.0583
5.4	1.10	1.07	1.03	0.0730	0.0539	0.0285
5.5	0.31	0.30	0.28	0.1120	0.0825	0.0434
5.6	0.05	0.05	0.04	0.4593	0.3365	0.1766
5.7	0.02	0.02	0.02	1.2249	0.8959	0.4658
5.8	0.02	0.02	0.02	0.7313	0.5344	0.2752
5.9	0.07	0.07	0.07	0.1365	0.0998	0.0515
6.0	0.29	0.28	0.27	0.0184	0.0135	0.0072
6.1	1.28	1.25	1.19	0.0079	0.0059	0.0033
6.2	5.07	4.97	4.71	0.0228	0.0165	0.0088
6.3	7.40	7.24	6.86	0.1738	0.1230	0.0633
6.4	1.91	1.86	1.78	0.5764	0.4047	0.2048
6.5	2.42	2.38	2.28	0.4481	0.3133	0.1573
6.6	2.03	1.99	1.91	0.2468	0.1733	0.0872
6.7	2.31	2.27	2.17	0.1221	0.0863	0.0438
6.8	1.67	1.64	1.57	0.0800	0.0572	0.0294
6.9	1.14	1.12	1.07	0.0527	0.0381	0.0200
7.0	1.46	1.43	1.37	0.0302	0.0220	0.0117
7.1	4.05	3.96	3.80	0.0121	0.0089	0.0048
7.2	7.34	7.18	6.89	0.0073	0.0054	0.0030
7.3	7.79	7.61	7.31	0.0068	0.0051	0.0028
7.4	6.70	6.55	6.29	0.0077	0.0057	0.0031
7.5	5.44	5.32	5.11	0.0092	0.0068	0.0037

unable to point at the Sun. At this time, a moderate active region was present on the disk. The observations in 1996 were obtained shortly after launch and should be indicative of instrument conditions that are relatively free from the effects of sensitivity degradation due to solar radiation. The November 1998 measurements should also show relatively few effects of degradation because the EIT was able to outgas many of the impurities trapped in the instrument and to anneal the CCD at relatively warm temperatures during the period of solar off-pointing.

Table XV presents the observed count rates (DN s^{-1}) for coronal-hole, quiet-Sun, and active-region emission and the predicted count rates. The predicted count rates are derived from the DEM values in the CHIANTI database. The most reliable comparison is probably for the quiet Sun. In February/March 1996 the disk was fairly uniform so the quiet-Sun values should be fairly typical. The DEM used to predict the intensities is derived from quiet-Sun EUV spectra from OSO-6 (Dupree *et al.*, 1973). For the 171 Å wavelength sector, the predicted intensities are factors of 1.12, 1.38, and 1.06 above the observed values for 1996, which are those most indicative of the quiet Sun. This difference is easily within the combined error budget of the EIT calibration and the derived DEM values. Landi *et al.* (1999) report line intensities for most of the strongest lines in the 171 Å band. Integrating their quiet-Sun intensities through the 171 Å response function predicts count rates (DN s^{-1}) of 240, 150 and 70 through the three filter-wheel positions. These are a factor of 2.2, 2.7 and 2.1 higher than the 1996 observed intensities but within the combined error budget for both experiments. Consequently, we are confident that the preflight calibration of the 171 Å channel is accurate to within the derived error estimates and free from serious errors. The total calibration error estimate for the 171 Å wavelength sector is the highest of the 4 due to the uncertainties in the mirror reflectivities.

For the 195 Å wavelength sector, there is good agreement between the observed (1996) and predicted quiet-Sun count rates. The predicted quiet-Sun intensities are factors of 0.75, 0.91, and 0.75 below the observed values for 1996. Consequently, these comparisons give us confidence that the preflight calibration of the 195 Å channel is accurate to within the derived error estimates and free from serious errors.

For the 284 Å wavelength sector, there is relatively good agreement between the observed (1996) and predicted count rates in the quiet Sun. The ratio of the predicted to observed values are 1.7, 1.6, and 0.7. However, the Fe XV line at 284 Å only accounts for a portion of the count rates for this sector in the quiet Sun. The agreement between the predicted and observed count rates in an active region is encouraging but because of the large range of active region intensities, it indicates the lack of gross errors in the preflight calibration for this channel. We find no significant reason to believe that our calibration of the 284 Å wavelength channel deviates from the actual value by more than its estimated error.

For the 304 Å wavelength sector, there are two entries. Because the observed intensity of the He II $\lambda 304$ lines (Dupree and Reeves, 1971; Warren, Mariska, and Lean, 1998) tends to be significantly greater than predicted by optically-thin, collisional-excitation models, there are two calculations for the predicted intensities. The first entry was obtained in the same manner as described above. The second entry was obtained by multiplying the collision rates in the CHIANTI database by the factor of 6 that is needed to reproduce observed intensities of He II $\lambda 304$. The ratio of the 304 Å intensities predicted with the modified CHIANTI database to the observed 1996 quiet-Sun intensities are 0.68, 0.92 and 1.8. There

TABLE XV

Comparison of predicted and observed EIT count rates (DN s^{-1}): 21 February–1 March 1996 and 5 November 1998. There are two entries for the 304 Å wavelength sector. For the first set, the predicted intensities have been calculated from the standard version of the CHIANTI database and for the second, the predicted intensities, in parentheses, have used a modified version of the CHIANTI database where the excitation rate of the He II $\lambda 304$ lines has been multiplied by a factor of 6.

Band	Filter	Coronal hole		Quiet Sun			Active region		
		Obs. 1996	Pred.	Obs. 1996	Obs. 1998	Pred.	Obs. 1996	Obs. 1998	Pred.
171 Å	Clear	33	25	110	183	123	510	930	1700
	Al+1	17	13	56	90	64	240	460	880
	Al+2	9.5	6.1	34	51	30	130	240	410
195 Å	Clear	17	3.7	44	120	33	420	760	1050
	Al+1	8.1	1.9	22	57	17	210	370	530
	Al+2	4.6	0.8	12	30	7.3	100	180	230
284 Å	Clear	0.68	0.46	1.0	6.7	1.7	15	84	69
	Al+1	0.34	0.17	0.46	2.0	0.62	5.8	28	25
	Al+2	0.19	0.041	0.24	1.0	0.14	1.5	8.2	5.6
304 Å	Clear	23	7.4	44	113	7.9	120	450	125
	Al+1	6.6	2.6	13	33	2.7	59	136	43
	Al+2	2.1	0.47	4.1	11	0.53	19	36	8.8
304 Å	Clear	23	(35)	44	113	(30)	120	450	(280)
	Al+1	6.6	(12)	13	33	(10)	59	136	(100)
	Al+2	2.1	(2.2)	4.1	11	(1.9)	19	36	(18)

is also good agreement between the observed active region intensities and the intensities predicted from the modified CHIANTI database. Consequently, these comparisons give us confidence that the preflight calibration of the 304 Å channel is accurate to within the derived error estimates and free from serious errors.

Acknowledgements

We would like to thank Dr J. Newmark for pointing out errors in a previous version. This work and NRL's participation in the construction and development of the EIT experiment, its calibration and data analysis have been supported by NASA.

References

- Arnaud, M. and Raymond, J. C.: 1992, *Astrophys. J.* **398**, 39.
- Arnaud, M. and Rothenflug, R.: 1985, *Astron. Astrophys. Suppl.* **60**, 425.
- Canfield, L. R., Kerner, J., and Korde, R.: *Applied Optics* **28**, 3940.
- Defise, J.-M. *et al.*: 1995, *SPIE* **2517**, 29.
- Delaboudinière, J.-P. *et al.*: 1995, *Solar Phys.* **162**, 291.
- Dere, K. P., Landi, E., Mason, H. E., Monsignori Fossi, B. C., and Young, P. R.: 1997, *Astron. Astrophys. Suppl. Series* **125**, 149.
- Dupree, A. K. and Reeves, E. M.: 1971, *Astrophys. J.* **165**, 599.
- Dupree, A. K. *et al.*: 1973, *Astrophys. J.* **182**, 321.
- Landi, E., Del Zanna, G., Breeveld, E. R., Landini, M., Bromage, B. J. I., and Pike, C. D.: 1999, *Astron. Astrophys. Suppl. Series* **135**, 171.
- Lemen, J. and Catura, R.: 1996, Solar Soft Tree
- Meyer, J. P.: 1985, *Astrophys. J. Suppl. Series* **57**, 173.
- Moses, D.: 1997, *Solar Phys.* **175**, 571.
- Song, X.: 1995, 'Characterization and Radiometric Calibration of the Solar Telescope EIT by Means of Synchrotron Radiation (between 10 and 100 nm)', Ph.D. thesis, University of Paris-South.
- Sutherland, R. S.: 1998, *Monthly Notices Royal Astron. Soc.* **300**, 321.
- Warren, H. P., Mariska, J. T., and Lean, J.: 1998, *J. Geophys. Res.* **103**, 12077.
- Windt, D. L.: 1998, *Comput. Phys.* **12**(4), 360.